iScience

A new approach in generating stable crack propagation at twisted bilayer graphene/hBN heterostructures

Graphical abstract

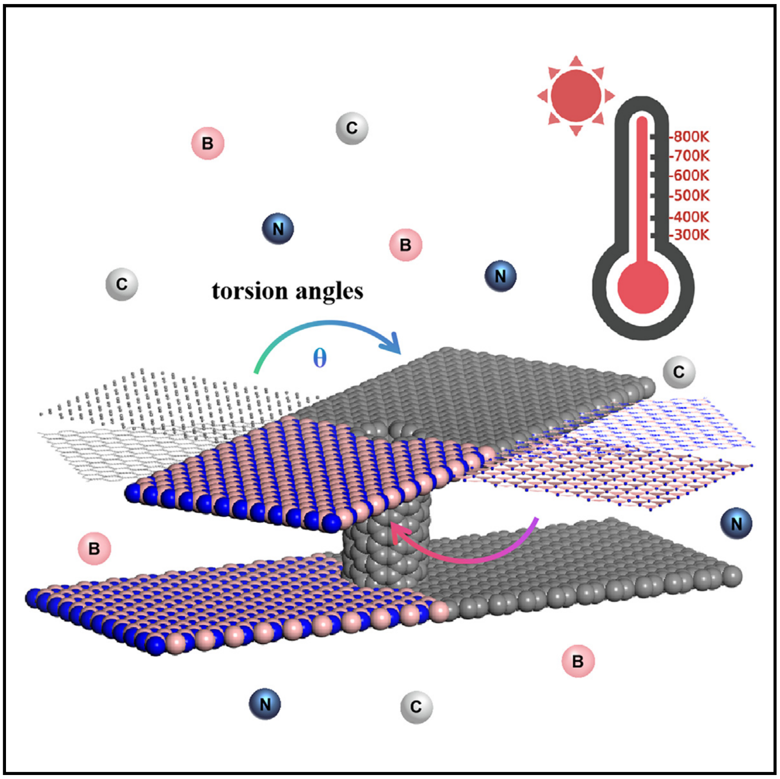

Authors

Lei Fan, Jinhao Zheng, Xinyu Cai

Correspondence

fanleigl@foxmail.com (L.F.),
baracyblabla@gmail.com (X.C.)

In brief

Physics; Condensed matter physics; Materials science

Highlights

- A possibility of unprecedented architecture may be opened up
- A temperature-dependent crack tip opening displacement model is established
- vdW heterostructure has additional practical benefits at high temperature

Fan et al., 2024, iScience *27*, 111387
December 20, 2024 © 2024 The Authors. Published by Elsevier Inc.
https://doi.org/10.1016/j.isci.2024.111387

CellPress

iScience

CellPress
OPEN ACCESS

Article

A new approach in generating stable crack propagation at twisted bilayer graphene/hBN heterostructures

Lei Fan,[1,2,4,*] Jinhao Zheng,[1] and Xinyu Cai[3,*]
[1]School of Civil Engineering and Architecture, Zhejiang University of Science & Technology, Hangzhou, P.R. China
[2]Zhejiang- Singapore Joint Laboratory for Urban Renewal and Future City, Hangzhou 310023, China
[3]Center for Reproductive Medicine and Obstetrics & Gynecology, Nanjing Drum Tower Hospital, The Affiliated Hospital of Nanjing University Medical School, Nanjing, China
[4]Lead contact
*Correspondence: fanleigl@foxmail.com (L.F.), baracyblabla@gmail.com (X.C.)
https://doi.org/10.1016/j.isci.2024.111387

SUMMARY

Thermodynamic theory suggests that the obvious mechanical behavior caused by temperature and interlayer angle will affect the physical properties of materials, such as mechanical properties and transportation behavior, and it is different from the behavior in three-dimensional bulk materials. We observe an abnormal physical effect of bilayer graphene/hexagonal boron nitride (G/BN)-carbon nanotube (CNT) heterostructures, with a normalized out-of-plane deformation and normalized bond angle percentage to almost several times higher those of pristine G/BN heterostructures (without CNT) at 700–800 K. Our combined finite element theory and molecular dynamics simulations confirmed that the combination of CNT and interlayer angle diverted and bridged the propagating crack and provided a stable crack propagation path and crack tip opening displacement, resulting in the stress fields to be controlled around the CNT at high temperature. It offers an ideal design for two-dimensional (2D) materials that can maintain exceptional mechanical properties in flexible device applications.

INTRODUCTION

In 2018, Y. Cao and P. Jarillo-Herrero et al. conducted an experiment to deflect the angles between the two layers of graphene.[1,2] They discovered that when the layers were twisted at a specific "magic angle," the bilayer graphene exhibited uncommon superconductivity. Since the concept of a magic angle twisted bilayer graphene was put forward, key words such as magic angle, superconductor and angular electronics have become research hotspots.[3–5] This distinctive feature stems from the atomic-scale Moiré superlattice structure, which modifies the electrical characteristics of bilayer graphene, facilitating the transition from an insulating state to a superconducting one.[6,7] In 2020, Z.Y. Zhang et al. established that the interplay phenomena between the pseudo-magnetic field and the highly correlated electronic states resulting from the lattice reconstruction in small-angle twisted double-layer graphene, along with the interlayer interaction, significantly impacts the structural reconstruction and property alterations of the system.[8]

Recently, researchers have expanded their investigation of twisted bilayer graphene to include twisted multi-layer graphene,[9] twisted bilayer hexagonal boron nitride (hBN),[10,11] and twisted bilayer graphene/hexagonal boron nitride (G/BN) heterostructures.[12,13]

In 2024, D. Goldhaber-Gordon et al. provided the first experimental observation of orbital ferromagnetism.[14] By using torsional force microscopy, open-face stack and cryogenic transport measurements methods to create samples with aligned G/BN moiré superlattices.

In their study, S. Jyoti Ray et al. employed the Ab-initio method to model and analyze the electrical, mechanical, and thermoelectric characteristics of G/BN heterostructure at different twisting angles. Their studies indicated that the G/BN heterostructure shows semiconducting nature at interlayer angles of 0°, 21.79°, and 38.21°.[15] Furthermore, these intricate heterostructures have exhibited exceptional mechanical characteristics, such as Young's modulus and bulk modulus, when the interlayer angles were controlled. In another work, the Young's modulus, bending rigidity, ultimate strength, and the fracture strain of bilayers heterogeneous G/BN structures were determined using reactive molecular dynamics.[16] Their results demonstrated that these layered heterostructures maintain their mechanical strength regardless of stacking order, and provide an in-depth understanding of the effect of layer ordering in separation or passivation applications.

The twisted bilayer graphene and G/BN typically exhibit exceptional in-plane rigidity, low-layer shear modulus, and remarkably low single-layer bending stiffness owing to their highly anisotropic atomic layer structure. Nevertheless, these attributes render twisted bilayer graphene, twisted bilayer G/BN, and multilayer Van der Waals (vdW) materials susceptible to curling, bubbling, and folding.[17] The thermodynamic theory

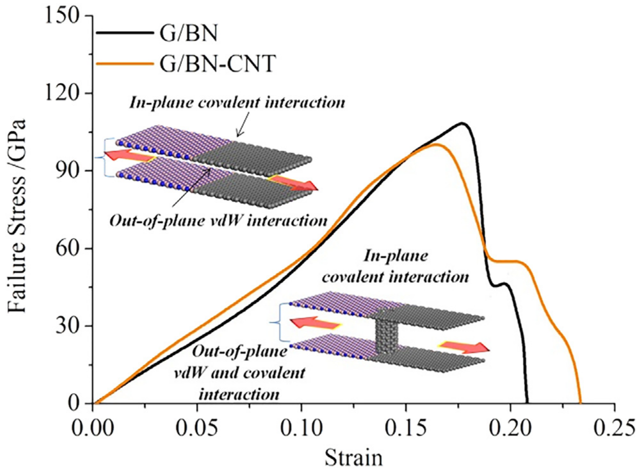

Figure 1. The stress-strain curves of the G/BN and G/BN-CNTs heterostructures

suggests that the combination of temperature-induced expansion can greatly enhance the internal stress level of vdW materials when thermal and mechanical factors are combined.[18] As a result, stress concentration, plastic deformation, crack propagation, fatigue failure, and other phenomena are more likely to occur, and lead to the degradation of mechanical properties and structural robustness.[19,20] The temperature related degradation of these interfacial mechanical properties has been fully reflected in twisted bilayer graphene, twisted bilayer hBN and other materials, especially in twisted bilayer G/BN heterostructures (key interface points).[21–23] More importantly, the coupling effect of temperature and interlayer angles on the local out-of-plane deformation and interfacial mechanical properties of twisted two-dimensional (2D) materials is more complicated, compared with the strengthening effect of positive Gaussian curvature and the weakening effect of negative Gaussian curvature.[24,25] The obvious mechanical behavior caused by temperature and interlayer angle will affect the physical properties of materials, such as mechanical properties and transportation behavior, and it is different from the behavior in three-dimensional bulk materials.[26–28]

In 2022, a coating with high thermal conductivity was prepared by modified h-BN, graphene and carbon nanotubes (CNTs) in the epoxy matrix.[29] The result shows the thermal conductivity of hBN-graphene-CNT/epoxy composite coatings is up to 5.65 $W \cdot (m^{-1} K^{-1})$ with a mixed filler content of 46 vol %. It can be attributed the fact that one-dimensional CNT is interspersed between graphene and hydroxylating h-BN due to its large aspect ratio, which plays a good role in connection of thermal conductive fillers. In 2024, a CNT is introduced into a Gr/hBN vdW heterostructure to form Gr/CNT/hBN sandwiched heterostructures via covalent bonding of a sandwich layer between Gr and hBN layers.[30] The result shows the presence of CNT effectively enhances the phonon coupling between Gr and hBN layers, resulting in an increase in the overlap factor of phonon density of states between Gr and hBN, thus reducing the interfacial thermal resistance of Gr and hBN.

Currently, the research in this field is in its early stages, and there is ample opportunity for improving the design of materials with superior mechanical properties at high temperatures using twisted bilayer two-dimensional materials.

Hence, it is imperative to conduct a quantitative analysis on how the interplay between temperature and interlayer angle affects the mechanical properties of twisted bilayer G/BN heterostructures. On this basis, a method to improve the mechanical properties of twisted bilayer G/BN heterostructures layers need be explored. It provides theoretical guidance for the preparation and application of twisted graphene in flexible nano devices.

In this paper, we built the bilayer G/BN mixed heterostructures combined with vdW forces and covalent bonds. In order to enhance the interlayer mechanical properties of bilayer G/BN mixed heterostructures under the condition of interlayer angels and high temperatures, we also inserted a CNT into the key interface region of bilayer G/BN mixed heterostructures, different cases have been investigated, including different kinds of interlayer twist angles (0°, 5°, 10°, 15°, 20°, 30°, 45°, 60°, 90°, and 180°), different temperature (300 K, 400 K, 500 K, 600 K, 700 K, and 800 K) and the coupling effects of internal and external fields. The mechanical parameters (interfacial interaction, interlayer shear behavior, and bonding energies), geometric deformation, atomic reconstruction, and crack propagation path in G/BN with CNT heterostructures are studied using the molecular dynamics method and fracture mechanics theory. The investigation focuses on the non-flat section effect. It offers an ideal design for two-dimensional materials that can maintain exceptional mechanical properties and stability when subjected to stress and temperature variations in flexible device applications.

RESULTS AND DISCUSSION

Effect of CNT in G/BN heterostructures

Figure 1 shows the stress-strain curves of the G/BN and G/BN-CNTs heterostructures. It is found that the stress-strain curves of G/BN and G/BN-CNT models can be divided into three change intervals. At an elastic deformation region in the small strain range $(0 < (strain(\varepsilon) < 0.02)$, the stress-strain curves in all cases show the characteristics of linear change.

With the increase of strain, the stress-strain curves of the two models began to show nonlinear stress, and their changing trend did not decrease, and the stress of the models could maintain a linear limit stress level in a strain interval. At the failure stage, the failure stress and strain of the G/BN model reached 111.79 GPa and 0.183, while the failure stress and strain of the G/BN-CNT model only decreased by 7.48% and 3.39%, compared with the G/BN model. This is because the existence of CNT triggers to the increase of initial distorted stress in G/BN model, and then leads to the decrease of failure stress and strain. On the contrary, there is an effective interface joints between G/BN vacancy and CNTs. These interface joints can provide a path of stress transfer, which provides an idea for increasing interlayer toughness and realizing stable cracks.

After that, the failure stress of G/BN and G/BN-CNT model suddenly dropped, and a yield platform with almost constant stress appeared briefly.

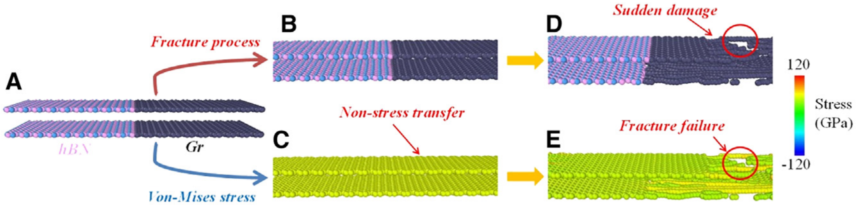

Figure 2. The crack propagation and stress distribution of G/BN heterostructures (without CNT)

(A) Initial stage, (B) crack propagation before cracking, (C) Von-Mises stress distribution before cracking, (D) fracture path after cracking, and (E) Von-Mises stress distribution after cracking.

In the G/BN model, a yield platform lasts for a short period, and the yield platform maintains a strain of 0.013 and a constant stress of less than 10%. Moreover, in the G/BN-CNT model, the duration of the yield platform is relatively long time (almost twice as long as that in the G/BN model), and the yield plateau maintains a strain of 0.024. A higher enhancement in duration of yield platform, relative to the G/BN model, can be attributed to the fact that the presence of CNTs induced a transformation from original sp^2 bonds to a mixture of sp^2 and sp^3 bonds, thus leading to the G/BN-CNT model having better toughness. Obviously, two different failure modes were found in G/BN and G/BN-CNT heterostructures.

One is that the G/BN in the two layers will not break at the same time due to the weak interactions of van der Waals force. Especially, the layer-by-layer fracture behavior of G/BN under external load is that the G/BN of one layer is broken first, and then the G/BN of the other layer is broken.

The other is that failure behavior of CNT-induced interlayer crosslinking when G/BN is pulled out. In the G/BN structure with cross-linking between CNT layers, the tensile load is mainly transferred through the CNT layers. With the G/BN structure being completely pulled out, the structure loses overlap, which leads to the destruction of the CNT network between G/BN layers, and finally the tensile stress decays rapidly, and the G/BN-CNT structure fails.

An important conclusion can be obtained that the vdW force is less than the interaction force of covalent bonds between layers (CNT and G/BN layer, C–N and C–B bonds), so the long-term interaction between interlayer atoms cannot be maintained.

Overall, the presence of interlayer stress can easily lead to a delamination failure, and interlayer delamination will seriously reduce the stiffness and strength of G/BN heterostructures. Therefore, interlayer stress and interlayer interaction are important issues that must be considered in the design of G/BN heterostructures.

The fracture behavior and stress distribution of G/BN and G/BN-CNT heterostructures have been shown in Figures 2 and 3.

As can be seen from Figure 2B, the G/BN heterostructure is uniformly stretched. Before reaching the stress limit, there is almost no out-of-plane deformation in the G/BN heterostructure. Von-Mises stresses can be calculated by the Equation 2.

According to the diagram of Von-Mises, the stresses are evenly distributed in the G/BN heterostructure (see Figure 2C). Obviously, there is no stress transfer in G/BN heterostructure due to the weakly vdW interlayer interaction. After rupture and failure, the crack appeared at the edge of G/BN heterostructure, and broke, and the structure was destroyed.

In considering the CNT in G/BN heterostructure, the distorted stresses were controlled near the CNT due to the stronger interlayer interaction of sp^2+sp^3 (see Figure 3C). The inhomogeneity of internal stress and strong interaction interface lead to the deflection of cracks (see Figures 3D and 3E). We find that the abnormal improvement of interfacial toughness comes from the localization of stress field and out-of-plane deformation at the G/BN-CNT interface caused by the CNT.

An important conclusion can be obtained that the presence of CNT changed the stress field distribution, controlled the crack propagation path, and greatly enhanced the toughness of graphene-based flexible materials.

CNT induced geometric effect in G/BN heterostructures

In order to have a deeper understanding of the different manifestations of B–N, C–B, and C–C bonds, such as stretching, bending, torsion, out-of-plane bending and vdW force interaction, etc., the change of bond length and bond angles of G/BN-CNT heterostructures with different cases at Cartesian coordinate based on continuum mechanics was shown as Figure 4.

It is confirmed that the existence of CNT leads to the redistribution of stress field at the interface junction, which comes from the change of bond lengths and bond angles. In G/BN heterostructures, the interlayer stress can easily lead to delamination failure, which will seriously reduce the stiffness and strength of G/BN heterostructures. However, in G/BN-CNT heterostructures, CNT can share the external force of G/BN heterostructures and act as a bridge between upper G/BN and lower G/BN layers. At the same time, it only leads to the stress reduction in the range of <10%.

Figure 5 shows the normalized out-of-plane deformation of G/BN and G/BN-CNT heterostructures under the different length ($\frac{x_1}{4}$, $\frac{x_1}{2}$, $\frac{3x_1}{4}$, $\frac{x_1+x_2}{2}$, $x_1 + \frac{x_2}{4}$, $\frac{x_2}{2}$ and $\frac{x_2}{4}$).

Regarding the normalized out-of-plane deformation at which the length of simulated model is recorded, it has been found that the normalized out-of-plane deformation of G/BN-CNT heterostructures is highly correlated with length of the model, while the normalized out-of-plane deformation of G/BN heterostructures is not sensitive to length of the model. Obviously, the highest value of normalized out-of-plane deformation is found at $\frac{x_1+x_2}{2}$ domain of G/BN-CNT heterostructures, the lowest value of normalized out-of-plane deformation is found at $x_1 + \frac{x_2}{4}$ domain of G/BN-CNT heterostructures. However, the normalized out-of-plane deformation of G/BN heterostructures does not follow the changing trend of G/BN-CNT heterostructures. As an illustration, the normalized out-of-plane deformation is 0.76–1 for the

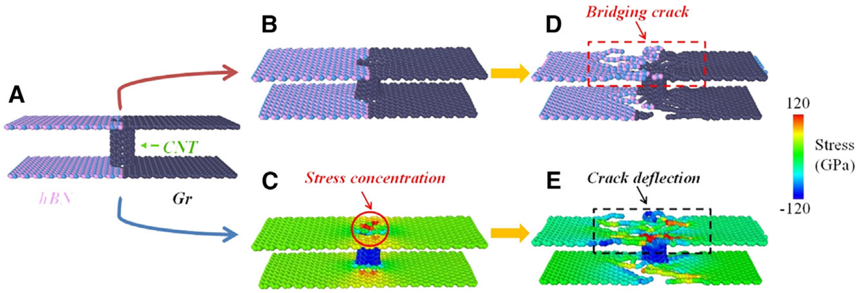

Figure 3. The crack propagation and stress distribution of G/BN heterostructures in presence of CNT

(A) Initial stage, (B) crack propagation before cracking, (C) Von-Mises stress distribution before cracking, (D) fracture path after cracking, and (E) Von-Mises stress distribution after cracking.

G/BN-CNT heterostructures, which is almost 4 times greater than its original form (G/BN). Furthermore, the presence of CNT can lead to a strengthen effect in normalized out-of-plane deformation of G/BN-CNT heterostructures due to the transformation of strong π bond into weak σ bond.

Based on the aforementioned analysis, the presence of CNT can effectively improve the bending stiffness of G/BN heterostructures and reduce the negative impact on the in-plane stress of G/BN heterostructures.

Effect of interlayer angles in G/BN-CNT heterostructures

There are many novel physical phenomena in vdW heterojunction, which are closely related to the interlayer twist angles, so it is particularly meaningful to regulate the vdW interaction between layers.[31,32]

Figures 6A and 6B show the effect of interlayer angles on the failure stress and strain of G/BN-CNT heterostructures. It is found that the interlayer angles have a great influence on the tensile properties of G/BN-CNT heterostructures.

Based on the results of Figures 6A and 6B , the tensile properties of G/BN-CNT heterostructures can be divided into four categories with the change of interlayer angles, including 0°–15°, 15°–30°, 30°–90°, and 90°–180°.

In considering the interlayer angles of 0°–15°, the failure stress and strain of G/BN-CNT heterostructures increase slowly, with a small change, with the increase of 4.95% and 2.83%, respectively. However, the highest failure stress and strain values, with a larger difference between interlayer angles (15°–30°), are achieved when an interlayer angle is 30° at G/BN-CNT heterostructures. Maybe, the mechanical mechanism in G/BN-CNT heterostructures could follow a trend of graphene with different chirality (armchair and zigzag). The failure stress and strain of graphene with zigzag is higher than those of graphene with armchair according to the previous studies.[33] Likewise, the presence of interlayer angles induced the changes of bond lengths and bond angles of G/BN layer, and has a certain angle with the stretching direction, obtaining partial chiral effect.

When the interlayer angles is increase from 30° to 90°, the failure stress and strain of the G/BN-CNT90° heterostructures decreases rapidly and remains at 90.12 GPa and 0.169, with a decrease of 25.55% and 10.65%, which decrease by 25.55% and 10.65%. This poor failure stress and strain is due to the weak stress transfer area under the external loading. That is the main reason why the G/BN-CNT90° heterostructures in simulated studies fail to achieve higher strength and interfacial interactions. When the G/BN-CNT90° heterostructures are under tension, only the partial area of upper G/BN layer fully participates in carrying the external loading since an interlayer angle was changed between the upper Gr/BN lattice and the tensile direction.

Next, we turn our attention to the effect of interlayer angles of 90°–180° on the failure stress and strain of G/BN-CNT heterostructures. Note that the failure strain of the G/BN-CNT0° heterostructures is 0.177 while it increases from 0.169 to 0.173 for G/BN-CNT heterostructures in the range of interlayer angles from 90° to 180°. When compared with the G/BN-CNT90° heterostructures, the presence of interlayer angle 180° results in improvement in 8.89% and 2.37% in failure stress and strain.

It is interesting that just like a roller coaster game, the failure stress and strain of G/BN-CNT heterostructures have changed greatly when the interlayer angles increase from 0° to 180°. Likewise, the presence of interlayer angles plays positive and negative effect in failure stress and strain of G/BN-CNT heterostructures.

On the basis of the foregoing analysis, it is confirmed that the interlayer angles affect the failure stress and strain of G/BN-CNT heterostructures in two contrary ways. On one hand, an appropriate angle between the tensile direction and G/BN lattice can slow down stress concentration and prevent crack propagation. On the other hand, an inappropriate interlayer angle will affect the effective stress transfer area, and then it is difficult to transfer the distorted stress of upper G/BN to lower G/BN through CNT. Obviously, the effective stress transfer area of G/BN-CNT90° is lower than that of G/BN-CNT180° and G/BN-CNT0°.

It is expected that the failure stress and strain of G/BN-CNT heterostructures will be controlled with introducing interlayer angles.

There are many novel physical phenomena in vdW heterostructures, which are closely related to the interlayer interaction, so it is particularly meaningful to regulate the vdW interaction between layers.

The fracture behavior and stress distribution of G/BN-CNT heterostructures with interlayer angles of 30°, 60° and 90°, have shown in Figures 7, 8, and 9.

In considering the CNT and interlayer angles in G/BN heterostructure, the fracture behavior and stress distribution of G/BN-CNT heterostructures with interlayer angles of 30°, 60°, and 90° are different. This is mainly due to the effect of the effective length of the bonds and thermal vibration of lattice in the direction of load. The fracture behavior and stress distribution of G/BN-CNT heterostructures are very dependent on the interlayer angles.

Furthermore, the presence of CNT and interlayer angles leaded the lattice distortion and stress concentration, which

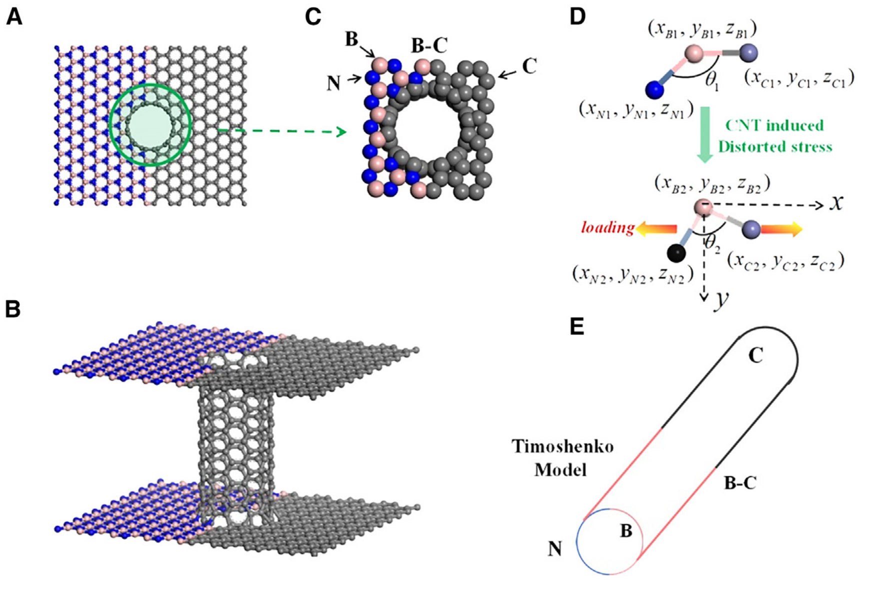

Figure 4. The change of bond length and bond angles of G/BN-CNT heterostructures with different cases at Cartesian coordinate based on continuum mechanics

(A) Perspective top-view of a portion of G/BN-CNT heterostructures with interlayer twist angle of 0°.

(B) Perspective side-view of a portion of G/BN-CNT heterostructures with interlayer twist angle of 0° (C) region of interface joint of G/BN layer and CNT.

(D) The change of bond length and bond angles at interface joint using Cartesian coordinate.

(E) Equivalent schematic diagram of beam element of G/BN layer and CNT.

makes the distribution of Z-direction stress extremely uneven along the CNT (see Figure 7). As a result, the propagation path of cracks will be controlled by the interlayer angles with the formation and propagation of cracks.

It can be also found that the stress concentration of the lower G/BN layer is obviously higher than that of the upper G/BN layer (see Figure 8C). This means that the upper layer area is still subjected to external load and does not participate in bearing. Compared with the G/BN-CNT heterostructures with interlayer angles of 30°, the stress concentration of the G/BN-CNT heterostructures with interlayer angles of 90° is relatively high, can be attributed to the fact that a lower Interlayer overlapping area and effective bonds number appeared at G/BN-CNT heterostructures with interlayer angles of 90°.

Although crack deflection and interlayer stress transfer will also occur in G/BN-CNT heterostructures with interlayer angles of 90°, the interlayer overlapping area and effective bonds number should also be considered. A key conclusion is that the hybrid sheets behave as a more toughness material when an appropriate interlayer angle is obtained.

Coupling effect of temperature and interlayer angles

Figure 10 shows the coupling effect of temperature and interlayer angles on the failure stress and strain of G/BN-CNT heterostructures. It is found from Figures 10A and 10B that the failure stress and strain of G/BN-CNT heterostructures in all cases decrease with the increase of temperature (from 300 to 800 K). In addition, the downward trends in failure stress and strain of G/BN-CNT heterostructures are similar to the temperature effect of single-layer graphene.[34] This is because the presence of CNT makes the upper G/BN layer and the lower G/BN layer became a whole similar to a house.

It is also confirmed that the in-plane interaction of covalent bonds mainly leads to the temperature-mechanical attenuation effect of G/BN-CNT heterostructures, but not the vdW force.

In considering the six kinds of temperature in G/BN-CNT heterostructures with different interlayer angles, the failure stress and strain parameters change very larger in each region (300–400 K, 400–500 K, 500–600 K, 600–700 K, and 700–800 K). Clearly, the change in each region of temperature related to failure strain can be divided into three parts: 300–600 K, 600–700 K, and 700–800 K.

In the range of 300–600 K, the failure strain and stress per K is reduced by nearly 5.31‱ and 4.15‱ because of the existence of interlayer angle of 0°. In addition, the presence of interlayer angle of 90° results also in average 5.73‱ and 4.35‱ in failure strain and stress.

Nevertheless, in the range of 600–700 K, an almost no angle of rotation achieved a higher reduction failure strain and stress per K, with a decrease of 14.28‱ and 10.59‱. Similar to G/BN-CNT0° heterostructures, the higher different is 14.41‱ and 10.92‱ for G/BN-CNT with the higher interlayer angle of 90°. Obviously, a remarkably reduction in failure strain and stress per K were found at high temperature of 600–700 K, relative to 300–600 K.

More surprisingly, in the range of 700–800 K, the presence of interlayer angle of 0° in G/BN-CNT heterostructures yields 11.76‱ decrease in failure strain per K and approximately a similar 12.04‱ decrease in failure stress per K. With regard to the failure strain and stress at which the G/BN-CNT90° heterostructures is measured, it is found that the G/BN-CNT90° heterostructures undergoes also a marginal 12.61‱ and 12.44‱ decrease in failure strain and stress per K.

Figure 11 shows the factor of stress attenuation of failure stress and strain at temperature area per K, including 300–400 K, 400–500 K, 500–600 K, 600–700 K and 700–800 K.

Clearly, all the failure stresses per K of G/BN-CNT possess a decreasing tendency with increasing the temperature, and the decreasing degree per K is dependent of the range of temperature (see Figure 11). However, the failure strain per K of G/BN-CNT in all cases did not follow the decline trend with failure stress per K. It is shown that the failure strain per K of G/BN-CNT in all cases first increases and then decreases when the temperature ranges from 300–600 K to 600–700 K and then to 700–800 K.

An important conclusion can be obtained that failure strain per K of G/BN-CNT heterostructures is very sensitive to the

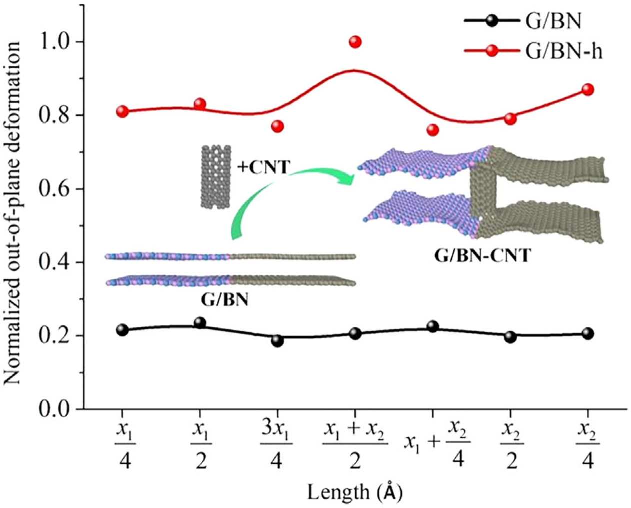

Figure 5. The normalized out-of-plane deformation of G/BN and G/BN-CNT heterostructures under the different length ($\frac{x_1}{4}$, $\frac{x_1}{2}$, $\frac{3x_1}{4}$, $\frac{x_1+x_2}{2}$, $x_1+\frac{x_2}{4}$, $\frac{x_2}{2}$, and $\frac{x_2}{4}$)

temperature. In other words, an abnormal physical effect (both high fracture toughness and larger limit failure strain) is found at G/BN-CNT heterostructures in the presence of interlayer angle. This unusual phenomenon can be understood by considering the critical bonds in CNT at the interface joint of G/BN layer that trigger failure.

The normalized out-of-plane deformations of G/BN-CNT heterostructures with interlayer angles (30°, 60°, 90°, and 180°) are shown in Figure 12.

In considering the different temperature, the normalized out-of-plane deformation parameters vary greatly. The normalized out-of-plane deformations of G/BN-CNT heterostructures increase considerably with the increase in the temperature. The degree of increase of the normalized out-of-plane deformations depends on the temperature. This is because the higher the temperature of the system, the stronger the thermal movement of atoms in the system.

At the temperature of 300 K, the lowest values for normalized out-of-plane deformations are obtained at G/BN-CNT heterostructures with interlayer angles of 90°. However, the highest values for normalized out-of-plane deformations are achieved at G/BN-CNT heterostructures with interlayer angles of 30°. Similar to the temperature of 300 K, the highest values for normalized out-of-plane deformations also obtained at G/BN-CNT heterostructures with interlayer angles of 30° under the temperatures (600 K and 800 K). The normalized out-of-plane deformations of G/BN-CNT heterostructures with interlayer angle do follow a regular and consistent trend with increase of temperature.

Bond lengths, angles, and energies under external physical field

To gain a deeper understand of the alterations in bond angles, bond lengths, and bond energies in G/BN-CNT with different interlayer angle heterostructures, it is necessary to investigate the impact of the superposition effect of the distorted stress field and the interaction between CNTs and G/BN heterostructures on geometrical deformation and bonding energies.

Based on Equations 19, 20, 21, 22, 23, and 24, the effects of temperature on the bond length, bond angle and their differential values of G/BN-CNT heterostructures with different interlayer angles (no CNT, 0°, 30°, 90°, and 180°) were calculated. Figure 13 shows the normalized differential values between bond length and bond angle with increasing the temperature.

It can be found from Figure 13 that the normalized differential values between bond length and bond angle (η_{nor}) in different cases of G/BN and G/BN-CNT heterostructures changes nonlinearly with the increase of temperature. In addition, the η_{nor} value of G/BN heterostructures is obviously larger than that of G/BN-CNT heterostructures with different cases. This means the increment of bond length in G/BN heterostructures is more sensitive to temperature, relative to G/BN-CNT heterostructures with different cases.

Clearly, the G/BN and G/BN-CNT heterostructures in different cases can be divided into three areas.

In considering the lower temperature (300–600 K), the η_{nor} values of G/BN and G/BN-CNT heterostructures increase slowly and keep a lower increment constant at almost 10% in per 100 K. Nevertheless, in the range of temperature of 600–700 K, the G/BN and G/BN-CNT heterostructures undergoes the significant 16.2%–25.2% increments in the η_{nor} values. When the G/BN-CNT heterostructures are subjected to the highest temperature (700–800 K), the G/BN-CNT heterostructures with no CNT, 0°, 30°, 90°, and 180° undergoes only a lower increment of almost 10%–15% in η_{nor} values, compared with temperature area of

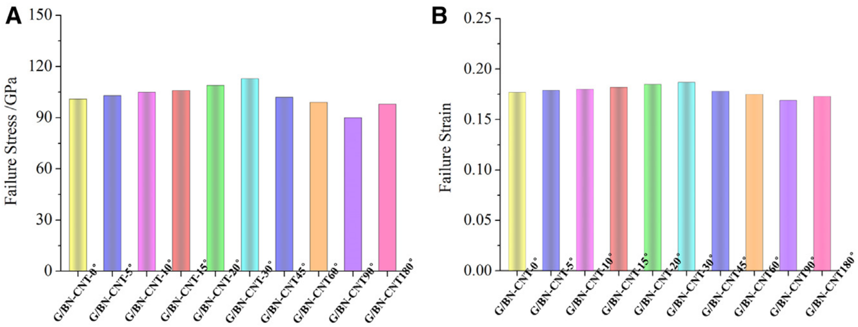

Figure 6. The mechanical properties of G/BN-CNT heterostructures with different cases of interlayer angles, including 0°, 5°, 10°, 15°, 20°, 30°, 45°, 60°, 90°, and 180°

(A) Failure stress of G/BN-CNT heterostructures with different cases of interlayer angles.

(B) Failure strain of G/BN-CNT heterostructures with different cases of interlayer angles.

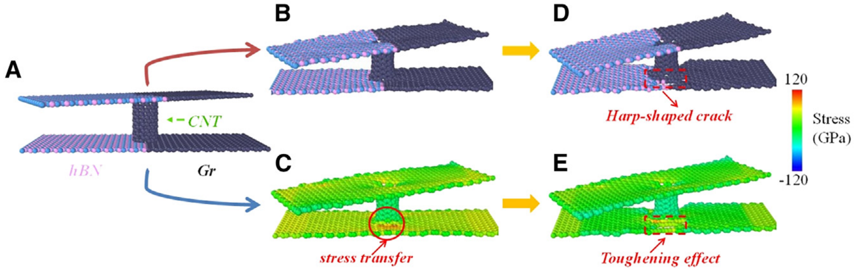

Figure 7. The crack propagation and stress distribution of G/BN-CNT heterostructures with interlayer angles of 30°

(A) Initial stage, (B) crack propagation before cracking, (C) Von-Mises stress distribution before cracking, (D) fracture path after cracking, and (E) Von-Mises stress distribution after cracking.

600–700 K. This result is consistent with the variation tendency of temperature related failure stress and strain.

In general, as the bond length is shorter, the bond energy is greater, the chemical bond is stronger and the mechanical properties are higher. In other words, the higher the temperature, the larger the vibration of atoms will be induced, the greater the decline and attenuation of inter-atomic bonding energy will be.

As the system temperature increases, the total kinetic energy of the system increases (see Equation 25). At low temperature, the kinetic energy of atoms is small, and the competition between bond length and bond angle in strain energy ratio is basically unaffected by thermal vibration. However, at high temperature, the greater the average energy of atomic thermal vibration is, the more dominant the competition of bond length in the strain energy ratio will be. As a result, the excellent in-plane elastic deformation of G/BN-CNT heterostructures with different interlayer angles is blocked and its in-plane stress is reduced.

Crack propagation and stress field

In the previous part, it is confirmed that the presence of CNT induced a geometric effect in the interface joint between G/BN layer and CNT due to the changes of bond lengths and bonds angles at interface joint. The studies have proved that interlayer angles changed the crystal lattice of the system. The local lattice structure rearrangement can cause changes in stress distribution of upper G/BN layer. In addition, the presence of interlayer angle makes the stress produce a component force at a certain angle with the tensile direction, which greatly reduces the probability of stress concentration. The stable crack propagation and stress concentration probability can be regulated by using interlayer angles.

On the basis of studies, the crack propagation of the upper G/BN layer is mainly decided by the interlayer angles and CNT, while the crack propagation of the lower G/BN layer is mainly influenced by CNT. These factors will lead to the difference of crack propagation between the upper layer and the lower layer.

In order to investigate the influence of external field (temperature) and internal field (interlayer angle) coupling on crack propagation and stress field at the crack tip of bilayer G/BN-CNT heterostructures, the energy release rate, stress intensity factor and crack propagation rate of G/BN-CNT heterostructures with interlayer angles were calculated by molecular dynamics, continuum theory and linear elastic fracture mechanics theory, and the interaction of factors affecting crack propagation path and rate was further discussed.

Figure 14 shows the crack initiation of G/BN-CNT heterostructures with interlayer angles (0°, 30°, 90°, and 180°) in fracture stage based on the finite element theory and molecular dynamic analysis. It can be found that the stress fields of all G/BN-CNT heterostructures are concentrated around CNT, then transferred to the crack tip and began to spread around.

In the non-interlayer angle (0°) (see Figures 14A–14C), the crack propagation path can be divided into two kinds. At the graphene domain, the crack tends to pass through the symmetrical hexagonal structure from top to bottom in a straight line, opening and bonding like a zipper. At the hBN domain, the crack propagation path will be deflected. This is mainly due to the asymmetry of hBN hexagonal structure and the stress contrast between boron and nitrogen atoms. The conclusion is consistent with the previous research results published in the journal "Nature."[35]

In the lower interlayer angle (30°) (see Figures 14D–14F), crack was found to deflect at the graphene domain due to the rotation of interlayer angles in the upper layer. The presence of interlayer angles raises the critical point for fracture of carbon bond at the graphene domain of upper layer, resulting in a longer effective length of carbon bonds. This means that additional energy is required to further promote crack propagation. What is even more surprising is that the crack at hBN domain undergoes a

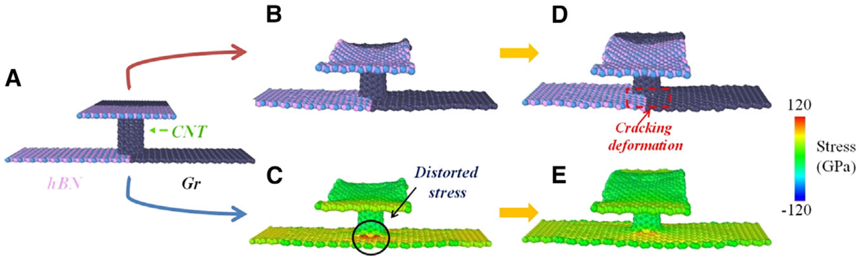

Figure 8. The crack propagation and stress distribution of G/BN-CNT heterostructures with interlayer angles of 90°

(A) Initial stage, (B) crack propagation before cracking, (C) Von-Mises stress distribution before cracking, (D) fracture path after cracking, and (E) Von-Mises stress distribution after cracking.

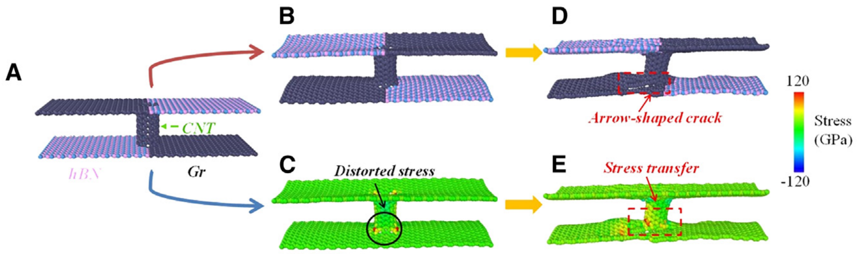

Figure 9. The crack propagation and stress distribution of G/BN-CNT heterostructures with interlayer angles of 180°

(A) Initial stage, (B) crack propagation before cracking, (C) Von-Mises stress distribution before cracking, (D) fracture path after cracking, and (E) Von-Mises stress distribution after cracking.

secondary deflection, which makes it more difficult for the crack to propagate and effectively enhances the toughness of the material. Different from the upper layer, the crack deflection of the lower layer is similar to Figures 14A–14C, but interlayer stress can also be transmitted from the lower layer to the upper layer due to the presence of CNTs. It greatly delayed the crack propagation speed, which can be confirmed by the crack propagation speed.

In the higher layer angle (90°), (see Figures 14G–14I), the crack propagation of G/BN-CNT-90° can be divided into two aspects. On the one hand, the presence of interlayer angles leads to lattice reconstruction in the upper layer. As a result, the actual number of covalent bonds being less than the nominal number of covalent bonds, leading to a significant reduction in stress and strain. On the other hand, local lattice structure rearrangement can cause changes in stress distribution, resulting in cracks propagating in the direction where the energy required for bond energy failure is relatively small (607 kcal/mol for C-C bond energy and 448 kcal/mol for B-N bond energy).[36]

In the highest layer angle (180°), (see Figures 14J–14L), the crack propagation of G/BN-CNT-180° did not undergo significant changes. Compared with the non-interlayer angle (0°), the direction of crack propagation has changed in the highest layer angle (180°). Specifically, crack deflection of G/BN-CNT-0° heterostructures is found at the left hBN region (see Figure 14B), while crack deflection of G/BN-CNT-180° heterostructures is found in the right hBN region (see Figure 14K).

Figure 15 shows the normalized average crack speed of G/BN-CNT heterostructures with different cases of interlayer angles. Figure 16 shows the normalized crack tip opening displacement of G/BN-CNT heterostructures with different cases of interlayer angles based on crack tip opening displacement model (see Figure 16B).

It can be seen from Figure 15 that the normalized average crack speed of all G/BN-CNT heterostructures increases with increasing the temperature. This is mainly because of ultra-high thermal vibration and local lattice reconstruction, which leads to the formation of instantaneous high stress bonds in the grains, and then the bonds break. In addition, the normalized average crack speed of G/BN-CNT-30° model is higher than that of G/BN-CNT-0° and G/BN-CNT-180° models. Compared with these two models (see Figure 14), the probability of stress concentration along the grain boundary direction could decrease at a suitable interlayer angle of 30°. When the crack gradually spreads to the next tensile region, the covalent bond in this region still has a high residual strength, which makes the crack need more energy to propagate. Herein, the degree of enhancement in the normalized average crack speed depends on the interlayer angles under the condition of high temperature.

Similar to the normalized average crack speed, the normalized crack tip opening displacement also degraded due to the presence of interlayer angle and temperature in G/BN-CNT heterostructures (see Figure 16A). A similar conclusion is obtained for the G/BN-CNT heterostructures with interlayer angles, i.e., the degree of reduction in the normalized crack tip opening displacement is closely related to the interlayer angles. The normalized crack tip opening displacement of the G/BN-CNT-30° model is 0.51 while it increases from 0.68 to 0.89 under the temperature range of 600 K and 800 K. When compared with the G/BN-CNT-0° model, the presence of interlayer angle of 30° results in 9.73% in the normalized crack tip opening displacement at the 300 K. In addition, the percentage of difference in G/BN-CNT-0° and G/BN-CNT-30° models is 9.73%

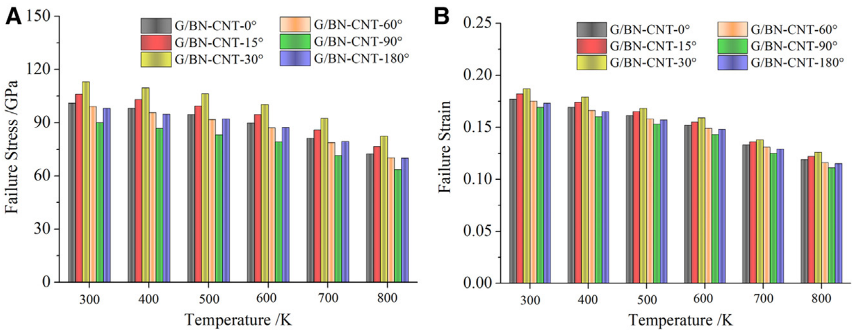

Figure 10. The mechanical properties of G/BN-CNT heterostructures with six cases of interlayer angles related to temperature, including 0°, 15°, 30°, 60°, 90°, and 180°

(A) Temperature dependence of failure stress and (B) temperature dependence of failure strain.

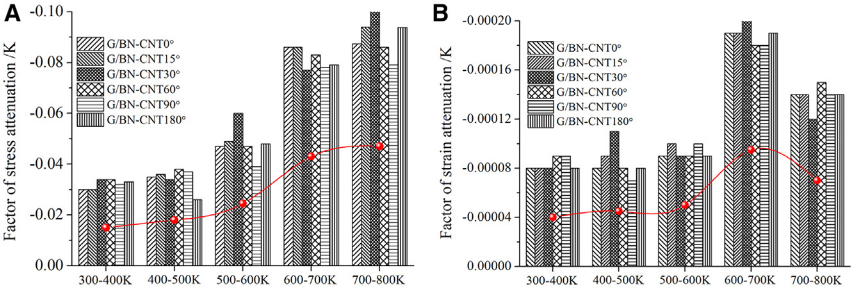

Figure 11. The factor of stress attenuation of failure stress and strain at temperature area per K, including 300–400 K, 400–500 K, 500–600 K, 600–700 K, and 700–800 K

(A) Stress attenuation factors at per K and (B) strain attenuation factors at per K.

(300 K) which is higher than that of G/BN-CNT-0 and G/BN-CNT-30 models (5.32%, 800 K). In other word, a relatively small of interlayer angle can achieve optimal the normalized crack tip opening displacement at 600–800 K.

According to the results of Figure 16A, the fitted curve for the influence of temperature on the opening displacement of structural crack tip can be calculated by following equation.

$$\frac{\delta'}{\delta} = e^{[0.01829\sim0.03064(T'-T)]} \qquad \text{(Equation 1)}$$

An important conclusion can be obtained that the normalized crack tip opening displacement of G/BN-CNT heterostructures with different cases of interlayer angles is sensitive to the temperature, because higher temperature makes it easier for atoms to leave the equilibrium position and more opportunities for defects.

Based on the aforementioned analysis, we can realize that the crack propagation can be controlled by appropriately adjusting the combination of interlayer angle and CNT, and allowing cracks to propagate along a predetermined path. More importantly, compared to G/BN heterostructures (without CNTs), the appropriate combination of CNT and interlayer angles can significantly reduce the possibility of stress concentration, improve interlayer stress transfer, and reduce crack propagation rate at high temperature.

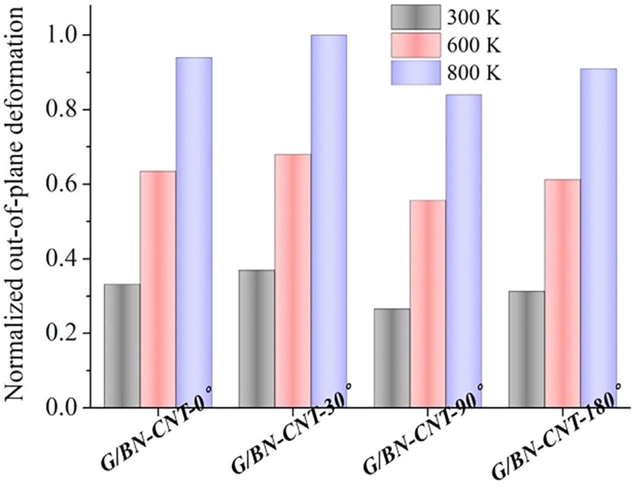

Figure 12. The normalized out-of-plane deformations of G/BN-CNT heterostructures with interlayer angles (30°, 60°, 90°, and 180°) under the conditions of temperature (300 K, 600 K, and 800 K)

Conclusion

In this paper, by combining the vdW forces and covalent bonds, the bilayer in-plane G/BN mixed heterostructures are constructed. Based on the weakly interlayer interaction and lower interfacial shear properties, a CNT is considered to insert into the bilayer in-plane G/BN mixed heterostructures. In order to quantitatively study the influence of the coupling effect of temperature and interlayer twist angle on the atomic reconstruction, interfacial mechanical properties and crack propagation path of G/BN-CNT heterostructures, different cases have been investigated, including different kinds of interlayer twist angles (0°, 5°, 10°, 15°, 20°, 30°, 45°, 60°, 90°, and 180°), different temperature (300 K, 400 K, 500 K, 600 K, 700 K, and 800 K) and the coupling effects of internal and external fields.

The main conclusions are summarized as follows.

(1) For the pristine G/BN without CNT, the interlayer interaction between G/BN layers are governed by the relatively weak vdWs forces and thereby the normalized out-of-plane deformation is as low as almost 0.2, and the normalized differential values between bond length and bond angle is as high as 0.61. However, the introduction of CNT can lead a positive effect in the normalized out-of-plane deformation and the normalized bond energies

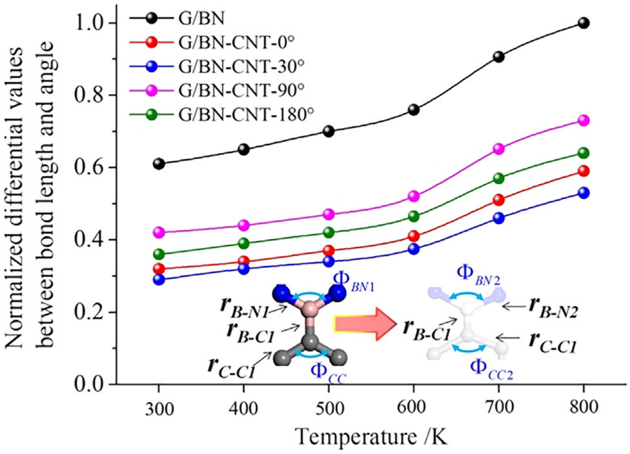

Figure 13. The normalized differential values between bond length and bond angle of G/BN-CNT heterostructures with interlayer angles (no CNT, 0°, 30°, 90°, and 180°) under the condition of different temperatures

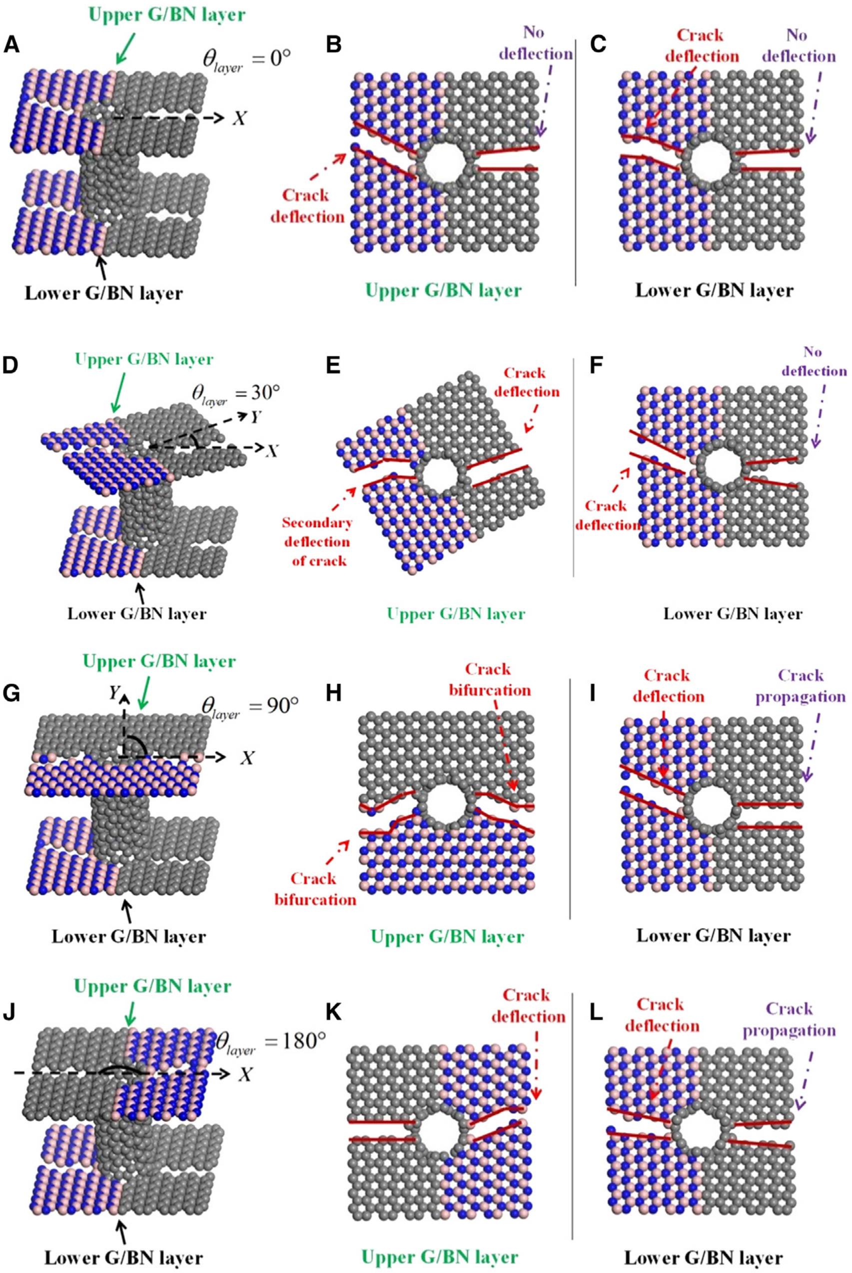

Figure 14. The crack initiation of G/BN-CNT heterostructures with interlayer angles (0°, 30°, 90°, and 180°) in fracture stage based on the finite element theory and molecular dynamic analysis

(A–C) Crack propagation of G/BN-CNT-0°.
(D–F) Crack propagation of G/BN-CNT-30°.
(G–I) Crack propagation of G/BN-CNT-90°.
(J–L) Crack propagation of G/BN-CNT-180°.

due to the stronger interlayer interaction and local lattice deformation induced by the CNT.

(2) All the failure stresses per K of G/BN-CNT possess a decreasing tendency with increasing the temperature, and the decreasing degree per K is dependent of the range of temperature. However, the failure strain per K of G/BN-CNT in all cases did not follow the decline trend with failure stress per K. When the temperature changes from 300–600 K to 600–700 K and then to 700–800 K, the unit K failure strain of G/BN-CNT heterostructure increases first and then decreases. In other words, in the case of interlayer angle, abnormal physical effect (high fracture toughness and greater ultimate failure strain) both appeared in G/BN-CNT heterostructure. This unusual phenomenon can be understood by considering the critical bonds in CNT at the interface joint of G/BN layer that trigger failure.

(3) By establishing the crack tip opening displacement model, it is found that the normalized crack tip opening displacement of g/BN-CNT heterostructure with different interlayer angles is sensitive to temperature, because higher temperature makes atoms leave the equilibrium position more easily and there are more opportunities for defects.

(4) Our combined finite element theory and molecular dynamics simulations confirmed that the combination of CNT and interlayer angle diverted and bridged the propagating crack, and provided a stable crack propagation path and crack tip opening displacement, which led to the stress fields around CNT being controlled at high temperature.

Based on the aforementioned analysis, we can realize that the crack propagation can be controlled by properly adjusting the combination of interlayer angle and CNT, and the cracks can be allowed to propagate along a predetermined path. More importantly, compared to G/BN heterostructure (without CNT), the proper combination of CNT and interlayer angles can significantly reduce the possibility of stress concentration, improve the interlayer stress transfer, and reduce crack growth rate at high temperature. It provides an ideal design for twisted two-dimensional materials, and can maintain excellent mechanical properties and stability when it is subjected to larger changes of stress and temperature in flexible equipment applications.

Limitations of the study

It is critical to recognize several limitations of this study. There are many adjustable variables in the initial conditions of the

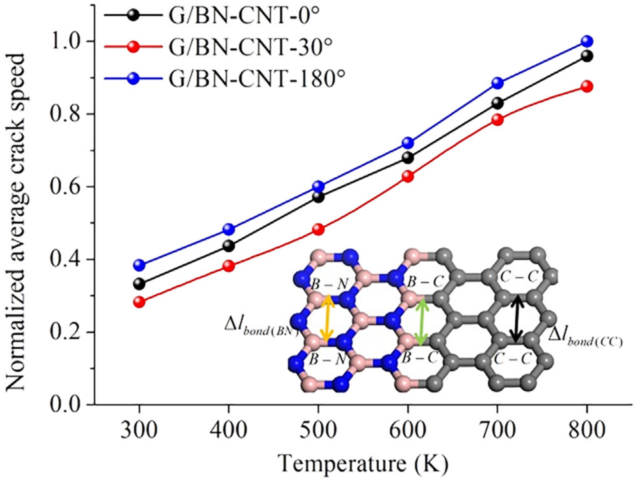

Figure 15. The normalized average crack speed of G/BN-CNT heterostructures with dfferent cases of interlayer angles (0°, 30°, and 180°)

simulation system, including the nanoholes size, CNT size, bond lengths between CNT and nanohole in the simulation system. The diameter of nanohole must be larger than that of CNT. Besides, the nanohole shape is approximately matched with the CNT shape. According to the aforementioned two requirements, a series of bond lengths between nanohole and CNT are considered.

The simulation work of generating stable crack propagation under different internal field such as CNT diameter, CNT height, and their induced buckling is still attractive due to the possibility of many interesting results, which are not represented in this paper.

Experimental validation of this simulation is very challenging. While our work has validated the feasibility of constructing bilayer graphene/hBN-CNT heterostructures using molecular simulation techniques and has provided insight into the atomic redistribution, geometry deformation at the molecular level, the limitations mentioned previously are indeed the ones that need to be remedied for further refinement of this work, and they will continue to be present in our subsequent research endeavors.

RESOURCE AVAILABILITY

Lead contact

Further information and requests for resources and information should be directed to and will be fulfilled by Lei Fan, (fanleigl@foxmail.com).

Materials availability

This study did not generate new unique reagents.

Data and code availability

- Raw data reported in this article will be shared by the lead contact upon request.
- This article does not report the original code.
- Any additional information required to reanalyze the data reported in this article is available from the lead contact upon request.

ACKNOWLEDGMENTS

These works were supported by Natural Science Foundation of Zhejiang Province (LQ23E080003), a Doctoral program of Zhejiang University of science and technology (F701104L08), and The Special Fund Project of Zhejiang University of Science and Technology's Basic Scientific Research Business Expenses in 2023 (2023QN016).

AUTHOR CONTRIBUTIONS

Conceptualization, L.F.; methodology, J.Z.; software, L.F. and J.Z.; formal analysis, L.F. and J.Z.; resources, L.F.; data curation, X.C.; writing – original draft, L.F.; writing – review and editing, L.F.; visualization, J.Z. and X.C.; supervision, X.C.; project administration, L.F.; funding acquisition, L.F.

DECLARATION OF INTERESTS

The authors declare no competing interests.

STAR★METHODS

Detailed methods are provided in the online version of this paper and include the following:

- KEY RESOURCES TABLE
- METHOD DETAILS
  - ○ System preparation
  - ○ Von-Mises stresses equation
  - ○ Geometric effect equations based on elastic mechanics theory
  - ○ Motion equations between C, B and N atom
  - ○ Relation equations for out-of-plane deformation
  - ○ Calculation equations for bond lengths, bond angles and bond energies

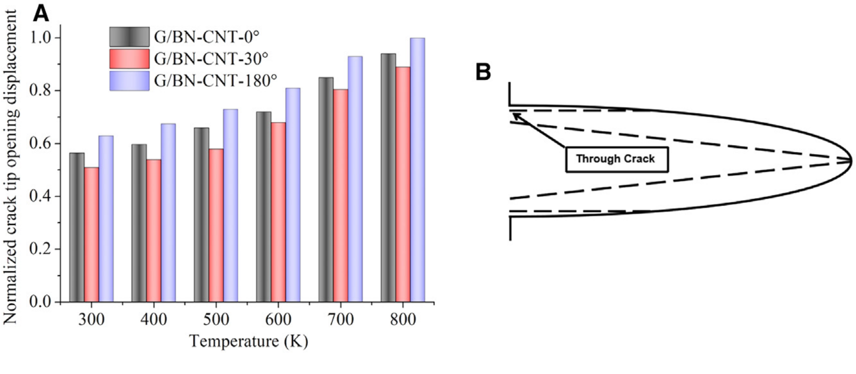

Figure 16. The normalized crack tip opening displacement of G/BN-CNT heterostructures with different cases of interlayer angles

(A) At the temperature (300–800 K), the normalized crack tip opening displacement of G/BN-CNT heterostructures, including 0°, 30°, and 180°.

(B) Crack tip opening displacement model.

  - ○ Calculation equations for kinetic energy and temperature of all atoms
  - ○ Crack propagation and stress field equations
- ● QUANTIFICATION AND STATISTICAL ANALYSIS
  - ○ Validation test

SUPPLEMENTAL INFORMATION

Supplemental information can be found online at https://doi.org/10.1016/j.isci.2024.111387.

Received: July 18, 2024
Revised: September 18, 2024
Accepted: November 11, 2024
Published: November 15, 2024

REFERENCES

1. Cao, Y., Fatemi, V., Fang, S., Watanabe, K., Taniguchi, T., Kaxiras, E., and Jarillo-Herrero, P. (2018). Unconventional superconductivity in magic-angle graphene superlattices. Nature *556*, 43–50. https://doi.org/10.1038/nature26160.
2. Cao, Y., Fatemi, V., Demir, A., Fang, S., Tomarken, S.L., Luo, J.Y., Sanchez-Yamagishi, J.D., Watanabe, K., Jarillo-Herrero, P., Taniguchi, T., et al. (2018). Correlated insulator behaviour at half-filling in magic-angle graphene superlattices. Nature *556*, 80–84. https://doi.org/10.1038/nature26154.
3. Sharpe, A.L., Fox, E.J., Barnard, A.W., Finney, J., Watanabe, K., Taniguchi, T., Kastner, M.A., and Goldhaber-Gordon, D. (2019). Emergent ferromagnetism near three-quarters filling in twisted bilayer graphene. Science *365*, 605–608. https://doi.org/10.1126/science.aaw3780.
4. Jiang, Y., Lai, X., Watanabe, K., Taniguchi, T., Haule, K., Mao, J., and Andrei, E.Y. (2019). Charge order and broken rotational symmetry in magic-angle twisted bilayer graphene. Nature *573*, 91–95. https://doi.org/10.1038/s41586-019-1460-4.
5. Lu, X., Stepanov, P., Yang, W., Xie, M., Aamir, M.A., Das, I., Urgell, C., Watanabe, K., Taniguchi, T., Zhang, G., et al. (2019). Superconductors, orbital magnets and correlated states in magic-angle bilayer graphene. Nature *574*, 653–657. https://doi.org/10.1038/s41586-019-1695-0.
6. Wong, D., Nuckolls, K.P., Oh, M., Lian, B., Xie, Y., Jeon, S., Watanabe, K., Taniguchi, T., Bernevig, B.A., and Yazdani, A. (2020). Cascade of electronic transitions in magic-angle twisted bilayer graphene. Nature *582*, 198–202. https://doi.org/10.1038/s41586-020-2339-0.
7. Zondiner, U., Rozen, A., Rodan-Legrain, D., Cao, Y., Queiroz, R., Taniguchi, T., Watanabe, K., Oreg, Y., von Oppen, F., Stern, A., et al. (2020). Cascade of phase transitions and Dirac revivals in magic-angle graphene. Nature *582*, 203–208. https://doi.org/10.1038/s41586-020-2373-y.
8. Shi, H., Zhan, Z., Qi, Z., Huang, K., Veen, E.v., Silva-Guillén, J.Á., Zhang, R., Li, P., Xie, K., Ji, H., et al. (2020). Large-area, periodic, and tunable intrinsic pseudo-magnetic fields in low-angle twisted bilayer graphene. Nat. Commun. *11*, 371. https://doi.org/10.1038/s41467-019-14207-w.
9. Park, J.M., Cao, Y., Watanabe, K., Taniguchi, T., and Jarillo-Herrero, P. (2021). Tunable strongly coupled superconductivity in magic-angle twisted trilayer graphene. Nature *590*, 249–255. https://doi.org/10.1038/s41586-021-03192-0.
10. Kim, D.S., Dominguez, R.C., Mayorga-Luna, R., Ye, D., Embley, J., Tan, T., Ni, Y., Liu, Z., Ford, M., Gao, F.Y., et al. (2024). Electrostatic moire potential from twisted hexagonal boron nitride layers. Nat. Mater. *23*, 65–70. https://doi.org/10.1038/s41563-023-01637-7.
11. Chiodini, S., Kerfoot, J., Venturi, G., Mignuzzi, S., Alexeev, E.M., Teixeira Rosa, B., Tongay, S., Taniguchi, T., Watanabe, K., Ferrari, A.C., and Ambrosio, A. (2022). Moiré modulation of van der Waals potential in twisted hexagonal boron nitride. ACS Nano *16*, 7589–7604. https://doi.org/10.1021/acsnano.1c11107.
12. Seo, Y., Masubuchi, S., Onodera, M., Moriya, R., Zhang, Y., Watanabe, K., Taniguchi, T., and Machida, T. (2022). Defect-assisted tunneling spectroscopy of electronic band structure in twisted bilayer graphene/hexagonal boron nitride moire superlattices. Appl. Phys. Lett. *120*, 203103. https://doi.org/10.1063/5.0084996.
13. Shi, B., Wang, H., Jiang, W., Feng, Y., Guo, P., Gao, H., Gao, Z., and Ren, W. (2023). Electric field effect of sliding graphene/hexagonal boron nitride heterobilayer. Appl. Surf. Sci. *636*, 157816. https://doi.org/10.1016/j.apsusc.2023.157816.
14. Kamat, R.V., Sharpe, A.L., Pendharkar, M., Hu, J., Tran, S.J., Zaborski, G., Jr., Hocking, M., Finney, J., Watanabe, K., Taniguchi, T., et al. (2024). Deterministic fabrication of graphene hexagonal boron nitride moiré superlattices. Preprint at arXiv. https://doi.org/10.1073/pnas.2410993121.
15. Gupta, N., Rani, S., Kumari, P., Ahuja, R., and Ray, S.J. (2023). Ultralow lattice thermal conductivity and thermoelectric performance of twisted Graphene/Boron Nitride heterostructure through strain engineering. Carbon *215*, 118437. https://doi.org/10.1016/j.carbon.2023.118437.
16. Mallick, G., and Elder, R.M. (2018). Graphene/hexagonal boron nitride heterostructures: Mechanical properties and fracture behavior from nanoindentation simulations. Appl. Phys. Lett. *113*, 121902. https://doi.org/10.1063/1.5047782.
17. Huang, Z., He, Z., Zhu, Y., and Wu, H. (2023). A general theory for the bending of multilayer van der Waals materials. J. Mech. Phys. Solid. *171*, 105144. https://doi.org/10.1016/j.jmps.2022.105144.
18. He, P., Du, T., Zhao, K., Dong, J., Liang, Y., and Zhang, Q. (2023). Lightweight 3D graphene metamaterials with tunable negative thermal expansion. Adv. Mater. *35*, 2208562. https://doi.org/10.1002/adma.202208562.
19. Raikwar, A., and Singh, S. (2024). Elastic properties and constitutive behaviour of graphene at finite temperature and large deformation. Eur. J. Mech. Solid. *105*, 105247. https://doi.org/10.1016/j.euromechsol.2024.105247.
20. Pacheco-Sanjuán, A., and Batra, R.C. (2024). Insights into the auxetic behavior of graphene: A study on the temperature dependence of Poisson's ratio and in-plane moduli. Carbon *215*, 118416. https://doi.org/10.1016/j.carbon.2023.118416.
21. Fan, L., Bian, Z., Huang, Z., Xia, Y., Song, F., and Xu, J. (2022). Role of grain boundary and nanoholes in geometrical deformation and bonding energies of graphene/hexagonal boron nitride. Diam. Relat. Mater. *126*, 109119. https://doi.org/10.1016/j.diamond.2022.109119.
22. Yang, X., and Zhang, B. (2023). Heterostrain and temperature-tuned twist between graphene/h-BN bilayers. Sci. Rep. *13*, 4364. https://doi.org/10.1038/s41598-023-31233-3.
23. Zhao, D., Fang, K., and Lian, Z. (2024). Mechanical and vibrational behaviors of bilayer hexagonal boron nitride in different stacking modes. Sci. Rep. *14*, 10619. https://doi.org/10.1038/s41598-024-61486-5.
24. Wang, J., Khosravi, A., Silva, A., Fabrizio, M., Vanossi, A., and Tosatti, E. (2023). Bending stiffness collapse, buckling, topological bands of freestanding twisted bilayer graphene. Phys. Rev. B *108*, L081407. https://doi.org/10.1103/PhysRevB.108.L081407.
25. Song, Z., Artyukhov, V.I., Wu, J., Yakobson, B.I., and Xu, Z. (2015). Defect-detriment to graphene strength is concealed by local probe: The topological and geometrical effects. ACS Nano *9*, 401–408. https://doi.org/10.1021/nn505510r.
26. Cong, C., and Yu, T. (2014). Enhanced ultra-low-frequency interlayer shear modes in folded graphene layers. Nat. Commun. *5*, 4709. https://doi.org/10.1038/ncomms5709.
27. Wang, J., Khosravi, A., Vanossi, A., and Tosatti, E. (2024). Colloquium: Sliding and pinning in structurally lubric 2D material interfaces. Rev. Mod. Phys. *96*, 011002. https://doi.org/10.1103/RevModPhys.96.011002.
28. Mogera, U., and Kulkarni, G.U. (2020). A new twist in graphene research: Twisted graphene. Carbon *156*, 470–487. https://doi.org/10.1016/j.carbon.2019.09.053.

29. Li, X., Wang, J., Tian, Y., Jiang, X., and Zhang, X. (2022). Thermal enhancement by constructing ordered-orienting hybrid network with modified boron nitride, graphene and carbon nanotubes in epoxy composite coatings. Prog. Org. Coating *172*, 107078. https://doi.org/10.1016/j.porgcoat.2022.107078.

30. Li 李, M.檬., Shakoori, M.A., Wang 王, R.瑞., and Li 李, H.海. (2024). Phonon thermal transport at interfaces of a graphene/vertically aligned carbon nanotubes/hexagonal boron nitride sandwiched heterostructure. Chin. Phys. Lett. *41*, 016302. https://doi.org/10.1088/0256-307X/41/1/016302.

31. Yoo, H., Engelke, R., Carr, S., Fang, S., Zhang, K., Cazeaux, P., Sung, S.H., Hovden, R., Tsen, A.W., Taniguchi, T., et al. (2019). Atomic and electronic reconstruction at the van der Waals interface in twisted bilayer graphene. Nat. Mater. *18*, 448–453. https://doi.org/10.1038/s41563-019-0346-z.

32. Chiodini, S., Kerfoot, J., Venturi, G., Mignuzzi, S., Alexeev, E.M., Teixeira Rosa, B., Tongay, S., Taniguchi, T., Watanabe, K., Ferrari, A.C., and Ambrosio, A. (2022). Moire modulation of van Der Waals potential in twisted hexagonal boron nitride. ACS Nano *16*, 7589–7604. https://doi.org/10.1021/acsnano.1c11107.

33. Zhao, H., Min, K., and Aluru, N.R. (2009). Size and chirality dependent elastic properties of graphene nanoribbons under uniaxial tension. Nano Lett. *9*, 3012–3015. https://doi.org/10.1021/nl901448z.

34. Zhang, Y.Y., and Gu, Y.T. (2013). Mechanical properties of graphene: Effects of layer number, temperature and isotope. Comput. Mater. Sci. *71*, 197–200. https://doi.org/10.1016/j.commatsci.2013.01.032.

35. Yang, Y., Song, Z., Lu, G., Zhang, Q., Zhang, B., Ni, B., Wang, C., Li, X., Gu, L., Xie, X., et al. (2021). Intrinsic toughening and stable crack propagation in hexagonal boron nitride. Nature *594*, 57–61. https://doi.org/10.1038/s41586-021-03488-1.

36. Huheey, J., and Cottrell, T. (1958). The Strengths of Chemical Bonds (Butterworths). https://doi.org/10.1016/j.actamat.2011.09.003.

37. Stukowski, A. (2010). Visualization and analysis of atomistic simulation data with OVITO-the Open Visualization Tool. Model. Simul. Mat. Sci. Eng. *18*, 015012. https://doi.org/10.1088/0965-0393/18/1/015012.

38. Smith, T.J., and Stevenson, K.J. (2004). Origin 7.5 OriginLab Corporation, One Roundhouse Plaza, Northampton, MA 01060. 1-800-969- 7720. price $699.00 (retail, singleuser), $489.00 (educational, single user). Contact company for other pricing options. J. Am. Chem. Soc. *126*, 6834. https://doi.org/10.1021/ja040926x.

39. Humphrey, W., Dalke, A., and Schulten, K. (1996). VMD: Visual molecular dynamics. J. Mol. Graph. *14*, 33–38. https://doi.org/10.1016/0263-7855(96)00018-5.

40. Thompson, A.P., Aktulga, H.M., Berger, R., Bolintineanu, D.S., Brown, W.M., Crozier, P.S., in 't Veld, P.J., Kohlmeyer, A., Moore, S.G., Nguyen, T.D., et al. (2022). LAMMPS-a flexible simulation tool for particle-based materials modeling at the atomic, meso, and continuum scales. Comput. Phys. Commun. *271*, 108171. https://doi.org/10.1016/j.cpc.2021.108171.

41. Fan, L., Cai, X., Wang, H., Ye, J., Hong, Y., and Ying, J. (2023). Toughening two-dimensional hybrid materials by integrating carbon nanotubes. Surface. Interfac. *36*, 102559. https://doi.org/10.1016/j.surfin.2022.102559.

42. Chaimovich, M., and Chaimovich, A. (2021). Relative resolution: A computationally efficient implementation in LAMMPS. J. Chem. Theory Comput. *17*, 1045–1059. https://doi.org/10.1021/acs.jctc.0c01003.

43. Fan, L., and Wang, F. (2024). Controllable toughness enhancement in graphene hybrid materials via planar twist-angle of carbon nanotubes. Comput. Mater. Sci. *233*, 112676. https://doi.org/10.1016/j.commatsci.2023.112676.

44. Kasra, E.E., Sadegh, S., and Maisam, J. (2018). Mechanical properties of defective hybrid graphene-boron nitride nanosheets: A molecular dynamics study. Comput. Mater. Sci. *149*, 170–181. https://doi.org/10.1016/j.commatsci.2018.03.023.

45. Fan, L., Bian, Z., Huang, Z., Xia, Y., Song, F., and Xu, J. (2022). Role of grain boundary and nanoholes in geometrical deformation and bonding energies of graphene/hexagonal boron nitride. Diam. Relat. Mater. *126*, 109119. https://doi.org/10.1016/j.diamond.2022.109119.

46. Si, C., Wang, X.D., Fan, Z., Feng, Z.H., and Cao, B.Y. (2017). Impacts of potential models on calculating the thermal conductivity of graphene using non-equilibrium molecular dynamics simulations. Int. J. Heat Mass Tran. *107*, 450–460. https://doi.org/10.1016/j.ijheatmasstransfer.2016.11.065.

47. Singh, J., and Kumar, R. (2023). Effect of the interface on mechanical and fracture properties of lateral graphene/hexagonal boron-nitride heterostructure: A molecular dynamics study. Diam. Relat. Mater. *136*, 110001. https://doi.org/10.1016/j.diamond.2023.110001.

48. Fan, L., Cai, X., Wang, H., Wang, F., and Song, F. (2024). Carbon nanotubes at the Graphene/hBN interface abnormally enhance its fracture toughness. Diam. Relat. Mater. *141*, 110662. https://doi.org/10.1016/j.diamond.2023.110662.

49. Gao, Y., Zhang, X., Jing, Y., and Hu, M. (2015). The unexpected non-monotonic inter-layer bonding dependence of the thermal conductivity of bilayered boron nitride. Nanoscale *7*, 7143–7150. https://doi.org/10.1039/C4NR07359B.

50. Fan, L., and Yao, W. (2019). Mechanical properties of a G/h-BN heterobilayer nanosheets coupled by interlayer sp3 bonds and defects. Mater. Res. Express *6*, 095075. https://doi.org/10.1088/2053-1591/ab2ec1.

51. Fan, L., and Yao, W. (2019). Effect of interlayer sp3 bonds and nanopores on mechanical properties of vertically-stacked 2D heterostructures. Mater. Res. Express *6*, 105618. https://doi.org/10.1088/2053-1591/ab3c44.

52. Neek-Amal, M., and Peeters, F.M. (2014). Graphene on boron-nitride: Moiré pattern in the van der Waals energy. Appl. Phys. Lett. *104*, 041909. https://doi.org/10.1063/1.4863661.

53. Iwata, T., and Shintani, K. (2018). Reduction of the thermal conductivity of a graphene/hBN heterobilayer via interlayer sp3 bonds. Phys. Chem. Chem. Phys. *20*, 5217–5226. https://doi.org/10.1039/C7CP07345C.

54. Odegard, G.M., Gates, T.S., Nicholson, L.M., and Wise, K.E. (2002). Equivalent-continuum modeling with application to carbon nanotubes. Compos. Sci. Technol. *62*, 1869–1880. https://doi.org/10.1016/S0266-3538(02)00113-6.

55. Kosmrlj, A., and Nelson, D.R. (2013). Mechanical properties of warped membranes. Phys. Rev. *88*, 012136. https://doi.org/10.1103/PhysRevE.88.012136.

56. Zhao, S., and Xue, J. (2013). Mechanical properties of hybrid graphene and hexagonal boron nitride sheets as revealed by molecular dynamic simulations. J. Phys. D Appl. Phys. *46*, 135303. https://doi.org/10.1088/0022-3727/46/13/135303.

57. Lee, C., Wei, X., Kysar, J.W., and Hone, J. (2008). Measurement of the elastic properties and intrinsic strength of monolayer graphene. Science *321*, 385–388. https://doi.org/10.1126/science.1157996.

58. Eshkalak, K.E., Sadeghzadeh, S., and Jalaly, M. (2018). Mechanical properties of defective hybrid graphene-boron nitride nanosheets: A molecular dynamics study. Comput. Mater. Sci. *149*, 170–181. https://doi.org/10.1016/j.commatsci.2018.03.023.

59. Bosak, A., Serrano, J., Krisch, M., Watanabe, K., Taniguchi, T., and Kanda, H. (2006). Elasticity of hexagonal boron nitride: inelastic X-ray scattering measurements. Phys. Rev. B *73*, 041402. https://doi.org/10.1103/PhysRevB.73.041402.

STAR★METHODS

KEY RESOURCES TABLE

REAGENT or RESOURCE	SOURCE	IDENTIFIER
Software and algorithms		
LAMMPS	Open source	www.lammps.org
Ovito	Stukowski et al.[37]	https://www.ovito.org/
Origin version 2019b	Smith et al.[38]	https://www.originlab.com
VMD version 1.9.3	Humphrey et al.[39]	https://www.ks.uiuc.edu/Research/vmd/

METHOD DETAILS

The simulation is implemented using LAMMPS, a parallel simulator for atomic and molecular systems on a large scale.[40–42]

The Tersoff potential is well-suited for accurately describing the characteristics of in-plane G/BN heterostructures and G/CNT heterostructures.[43–45] In addition, the Tersoff potential has shown remarkable effectiveness in simulating systems containing carbon (C), nitrogen (N), and boron (B), such as hBN, G, and CNT.[46–48] Therefore, the Tersoff potential was employed to describe the close-range interaction among carbon (C), nitrogen (N), and boron (B) atoms.[49,50] The Lennard Jones (LJ) potential is demonstrated by employing long-range interactions between carbon (C), nitrogen (N), and boron (B) atoms.[51]

The precision of G/BN-CNT interaction strength in heterostructures with interlayer twist angles is characterized by the definition of several atom types. The upper layer of G/BN contains C, B, and N atoms, which are designated as groups 1, 2, and 3, respectively. Consequently, the carbon (C), boron (B), and nitrogen (N) atoms in the top graphene/boron nitride (G/BN) layer are categorized as groups 4, 5, and 6, respectively. It is observed that atoms belonging to groups 1 to 6 are not bonded to CNT. In addition, the carbon atoms in carbon nanotubes (CNT) are designated as group 7.

Table S1 presents the attributes of the Lennard-Jones potential that regulate the interactions among C, N, and B atoms.[52,53] Table S2 displays the usage of the Tersoff and LJ potential. The chapter offers precise definitions for atomic groups spanning from 1 to 3. The LJ potential is used to describe the long-range interaction between the graphene/boron nitride (G/BN) layer and carbon nanotubes (CNT).

In order to have the ability to freely adjust the distance between layers, we opted to utilize the free boundary condition in the Z coordinate. Furthermore, the periodic boundary conditions are employed in both the X and Y coordinates. The equations governing the motion of atoms are numerically solved using a time step of 0.5 femtoseconds, which guarantees accurate preservation of energy. The initial structure is initially stabilized in the NVT ensemble using the Nosé-Hoover thermostat at a temperature of 300 K for a duration of 2 nanoseconds.

System preparation

We built the bilayer G/BN mixed heterostructures combined with vdW forces and covalent bonds, as shown in Figure S1. At the bilayer G/BN mixed heterostructures, the sizes of hBN layer in the bilayer G/BN mixed heterostructures are 42 Å × 28 Å, while the dimensions of G layer in the bilayer G/BN mixed heterostructures are 41 Å × 27 Å.

Subsequently, we constructed a nanohole with a radius of 11.36 Å at the interface region of the bilayer G/BN mixed heterostructures. Ultimately, a carbon nanotube (CNT) was inserted into the bilayer G/BN mixed heterostructures, resulting in the formation of bilayer G/BN heterostructures with CNTs (G/BN-CNT) (See Figure S2). It should be noted that the diameter (R_z) of CNTs is smaller than the width of the nanoholes.

To simulate the effect of interlayer twist angles on the key mechanical parameters of G/BN-CNT heterostructures, we have considered ten different twist angles (0°, 5°, 10°, 15°, 20°, 30°, 45°, 60°, 90° and 180°) , as illustrated in Figure S3.

In order to construct the initial heterostructures of G/BN-CNT with ten different interlayer twist angles, the interlayer distance d (Refer to Figure S2) is initially set to the height of CNT (6, 6). Once the simulated models reach a stable state, the interlayer distance will be automatically adjusted to an optimal value based on the covalent bond force between CNT and G/BN layers, as well as the van der Waals force. The diameter of CNT (6, 6) is 8.06 Å. If effective connection between CNT and nanohole is to be realized, the diameter of nanohole must be larger than that of CNT. Besides, the nanohole shape is approximately matched with the CNT shape. According to the above two requirements, a series of bond lengths between nanohole and CNT are considered. In order to achieve ideal stability of bond lengths and bond energies, the bond lengths between nanohole and CNT are set to 1.158-1.191 Å (See Figure S4).

Von-Mises stresses equation

Von-Mises stresses can be defined by the following Equation 2:

$$\sigma_{Von-Mises} = \sqrt{\frac{(\sigma_1 - \sigma_2)^2 + (\sigma_1 - \sigma_3)^2 + (\sigma_2 - \sigma_3)^2}{2}} \qquad \text{(Equation 2)}$$

Where σ_1, σ_2 and σ_3 are defined as the first, secondary, and tertiary principal stresses, respectively.

Geometric effect equations based on elastic mechanics theory

According to the classical elastic mechanics theory, the presence of CNT induced a geometric effect in the interface joint of G/BN layer and CNT due to the changes of bond lengths and bonds angles at interface joint. Herein, the geometric effect caused by distorted stress should be considered. Through the combination of distorted stress field of CNT and G/BN layer, the stress field distribution in G/BN-CNT with different interlayer angles can be calculated. In detail, the change of bond lengths and bond angles at interface joint (Induced CNT) can be regarded a dislocation, and the distorted stress field caused by a dislocation can be expressed by Cartesian coordinate (See Figure 8) Equations 3, 4, and 5:

$$\frac{\sigma_{xx}}{\beta\nu} = \frac{1}{2} ln \frac{S^2}{x^2+y^2} - \frac{y^2}{x^2+y^2} \qquad \text{(Equation 3)}$$

$$\frac{\sigma_{yy}}{\beta\nu} = \frac{1}{2} ln \frac{S^2}{x^2+y^2} - \frac{x^2}{x^2+y^2} \qquad \text{(Equation 4)}$$

$$\frac{\sigma_{xy}}{\beta\nu} = \frac{xy}{x^2+y^2} \qquad \text{(Equation 5)}$$

Where S is the area of interface joint of G/BN layer and CNT; $\beta > 0$ is the amplitude of the distorted stress field; ν is the size of the dislocation angle; positive dislocation is $\nu > 0$ and negative dislocation is $\nu < 0$.

A dislocation can be decomposed into a pair of dislocation dipoles. Based on the above stress field distribution, the positive dislocation position along the y direction is located at $(0, \Delta)$, the negative dislocation position along the y direction is located at $(0, -\Delta)$, and $\Delta > 0$. The built-in distorted stress field is expressed by following Equations 6, 7, and 8:

$$\frac{\sigma_{xx}}{\beta} = \frac{1}{2} ln \frac{x^2+(y-\Delta)^2}{x^2+(y-\Delta)^2} + \frac{x^2}{x^2+(y-\Delta)^2} - \frac{x^2}{x^2+(y+\Delta)^2} \qquad \text{(Equation 6)}$$

$$\frac{\sigma_{yy}}{\beta} = \frac{1}{2} ln \frac{x^2+(y+\Delta)^2}{x^2+(y-\Delta)^2} + \frac{x^2}{x^2+(y-\Delta)^2} - \frac{x^2}{x^2+(y+\Delta)^2} \qquad \text{(Equation 7)}$$

$$\frac{\sigma_{xy}}{\beta} = \frac{x(y-\Delta)}{x^2+(y-\Delta)^2} - \frac{x(y+\Delta)}{x^2+(y+\Delta)^2} \qquad \text{(Equation 8)}$$

Considering that the distance between positive and negative dislocations is very small, that is, 2 Δ is small enough, the stress field of a dislocation can be simplified by following Equations 9, 10, and 11:

$$\frac{\sigma_{xx}}{\beta} = \frac{y(3x^2+y^2)}{(x^2+y^2)^2} \qquad \text{(Equation 9)}$$

$$\frac{\sigma_{xy}}{\beta} = \frac{y(x^2-y^2)}{(x^2+y^2)^2} \qquad \text{(Equation 10)}$$

$$\frac{\sigma_{xy}}{\beta} = \frac{x(x^2-y^2)}{(x^2+y^2)^2} \qquad \text{(Equation 11)}$$

The in-plane principal stress (σ_{joint}) of system along the y direction can be obtained by the following Equation 12:

$$\sigma_r = \beta \frac{y}{x^2+y^2} \qquad \text{(Equation 12)}$$

Based on continuum mechanics, the above Equations is improved to be applicable to G/BN-CNT configuration. In G/BN layer, it can be divided into two parts: hBN (length x_1 in left direction) and G (length x_2 in right direction).

The strain of BN domain and G domain can be calculated by the following Equations 13 and 14:

$$\sigma_{G|x_2} = E_{G|x_2}\left(\varepsilon_{G|x_2} + \delta_{G|x_2}\sigma_{exter}\right) \tag{Equation 13}$$

$$\sigma_{BN|x_1} = E_{BN|x_1N}\left(\varepsilon_{BN|x_1} + \delta_{BN|x_1}\sigma_{exter}\right) \tag{Equation 14}$$

Where $\varepsilon_{BN|x_1}$ is the strain of BN domain in x_1 length and $\varepsilon_{G|x_2}$ is the strain of G domain in x_2 length. $\delta_{BN|x_1}$ and $\delta_{G|x_2}$ are the Passion ratios of BN and G domains. $E_{BN|x_1}$ and $E_{G|x_2}$ are the Young's modulus of h-BN and Gr domains. σ_{exter} is the tensile stress along the direction of external loading.

Motion equations between C, B and N atom

The motions between C, B and N atom are determined by the interaction force field, which is called space potential energy. The size of space potential energy depends on the relative position between C, B and N atom.[54] Space potential energy consists of the following parts.

$$U = \sum U_r + \sum U_\theta + \sum U_\phi + \sum U_\omega + \sum U_{vdW} \tag{Equation 15}$$

Where U_r is tensile potential energy and U_θ is planar bending potential energy. U_ϕ is dihedral angular torsional potential energy, U_ω is off-plane torsional potential energy and U_{vdW} is vdW force potential energy.

Among them,

$$U_r = \frac{1}{2}k_r(\Delta r)^2$$

$$U_\phi = \frac{1}{2}k_\phi(\Delta\phi)^2$$

$$U_\delta = \frac{1}{2}k_\delta(\Delta\gamma)^2 \tag{Equation 16}$$

Where k_r, k_ϕ and k_δ are three force constants, corresponding to the tension, bending and torsion of the bond respectively. Δr, $\Delta\phi$ and $\Delta\gamma$ are the change of bond length, bending angle and torsion angle.

Relation equations for out-of-plane deformation

According to the statistical mechanics theory,[55] the out-of-plane deformation induced by CNT will change equivalent tensile and bending stiffness of G/BN heterostructures. In addition, the in-plane Young's modulus, rigidities and bending rigidities can be expressed by using following Equations 17 and 18.

$$T_k, T_{n-k} \sim \sqrt{E_k d^2/T} \tag{Equation 17}$$

$$Y_k, G \sim \sqrt{T/E_k d^2} \tag{Equation 18}$$

Where T_k is renormalized bending rigidities, T_{n-k} is renormalized Gauss bending rigidities, T is bending rigidities, E_r is regional Young's modulus, G is shear rigidities and d is out-of-plane displacement.

Calculation equations for bond lengths, bond angles and bond energies

According to the above distorted stresses and bonding energies theory, the CNTs induced the changes of bond angles, bond lengths and bond energies in overlapping area of upper and lower G/BN layers can be calculated by using the following Equations 19, 20, 21, and 22.

$$r_{G\sim bond} = i\sum_{q=1}^{3}\int_{r_{C_0}}^{r_{Cq}} \frac{1}{2} f_C \sin\Phi_C dr_C \tag{Equation 19}$$

$$r_{BN\sim bond} = i\sum_{q=1}^{3}\int_{r_{B_0}}^{r_{Bq}} \frac{1}{2} f_B \sin\Phi_B dr_B + j\sum_{q=1}^{3}\int_{r_{N_0}}^{r_{Nq}} \frac{1}{2} f_N \sin\Phi_N dr_N \tag{Equation 20}$$

$$\Phi_{G\sim angle} = i\sum_{q=1}^{3}\int_{\Phi_{C_0}}^{\Phi_{Cq}} M_C\Phi_C d\Phi_C \tag{Equation 21}$$

$$\Phi_{BN\sim angle} = i\sum_{q=1}^{3}\int_{\Phi_{B_0}}^{\Phi_{Bq}} M_B\Phi_B d\Phi_B + J\sum_{q=1}^{3}\int_{\theta_{\Phi_0}}^{\Phi_{Nq}} M_N\Phi_N d\Phi_N \tag{Equation 22}$$

Where *f* represents the force on the covalent bonds and *M* is the bending moment of the covalent bond angles. Φ_{C_0}, Φ_{B_0} and Φ_{N_0} are the initial bond lengths of C, B and N atom, respectively. Φ_{C_q}、 Φ_{B_q} and Φ_{N_q} are the bond angles C, B and N during external loading, respectively. r_{C_0}, r_{B_0} and r_{N_0} are the initial bond lengths of C, B and N atom, respectively. r_{C_q}、 r_{B_q} and r_{N_q} are the bond lengths of C, B and N during external loading, respectively. $r_{G\sim bond}$ is the bond lengths change in G domain affected by CNT. $r_{BN\sim bond}$ is the bond lengths change in BN domain affected by CNT. $\Phi_{G\sim angle}$ is the bond angles change in G domain affected by CNT. $\Phi_{BN\sim angle}$ is the bond angles change in BN domain induced by CNT.

So, the differential value (η) between bond lengths and bond angles related to strain can be expressed.

$$\eta = \Delta r_p - \Delta\Phi_p \tag{Equation 23}$$

Where Δr_p is the values of bond lengths in the model that varies with strain. $\Delta\Phi_p$ is the values of bond angles in the model that varies with strain.

The normalized differential values between bond length and bond angle can be calculated by using following Equation:

$$\eta_{nor} = \frac{\eta_i}{\eta_{max}}\ (i = 1,2,3\cdot\cdot\cdot n) \tag{Equation 24}$$

Where η_{nor} is the normalized differential values between bond length and bond angle. η_{max} is the maximum value of all cases. η_i is the differential values between bond length and bond angle in simulated samples.

Calculation equations for kinetic energy and temperature of all atoms

According to the thermodynamic theory, the kinetic energy and temperature of all atoms in the system can be expressed by following Equation 25.

$$E_k = \sum_{i=1}^{N}\frac{1}{2}m_i v_i^2 = \frac{3}{2}N_{atom}k_B T \tag{Equation 25}$$

Where E_k is total kinetic energy of G/BN and G/BN-CNT heterostructures. N_{atom} is total atomic number of simulated models. k_B is boltzmann constant and *T* is thermodynamic temperature.

Crack propagation and stress field equations

According to the classical continuum theory, the length *c* of the plastic zone at the crack tip is:

$$c = l\left(sec\frac{\pi l}{2\sigma_s} - 1\right) \tag{Equation 26}$$

Where *l* is the length of the simulated model, σ_s is the yield stress acting on the interface between plastic zone and elastic zone.

The crack tip opening displacement at temperature (*T*) can be expressed by following Equation.

$$\delta = \frac{8\sigma_s l}{E\pi} lnsec\left(\frac{\pi\sigma_{loading}}{2\sigma_s}\right) \tag{Equation 27}$$

Where *E* is Young' modulus and $\sigma_{loading}$ is the external loading.

Finally, the formula for the influence of temperature on the opening displacement of structural crack tip is:

$$\frac{\delta'}{\delta} = \frac{\sigma_s' lnsec\left(\frac{\pi\sigma_{loading}}{2\sigma_s'}\right)}{\sigma_s lnsec\left(\frac{\pi\sigma_{loading}}{2\sigma_s}\right)} \tag{Equation 28}$$

Where δ' is the crack tip opening displacement at temperature (T'). σ_s' is the yield stress acting on the interface between plastic zone and elastic zone at temperature (T').

In addition, the crack speed of G/BN-CNT heterostructures with different cases of interlayer angles can be calculated.

$$V_{bond(CC)} = \frac{\Delta l_{bond(CC)}}{t_2 - t_1}, V_{bond(BN)} = \frac{\Delta l_{bond(BN)}}{t_2 - t_1}, V_{bond(BC)} = \frac{\Delta l_{bond(BC)}}{t_2 - t_1} \qquad \text{(Equation 29)}$$

$$V_{bond(nor)} = \frac{V_{bond(i)}}{V_{bond(max)}} = \frac{V_{bond(BN)}, V_{bond(BC)}, V_{bond(CC)} \sim N_{(bond)}}{V_{bond(max)}} \qquad \text{(Equation 30)}$$

Where $V_{bond(nor)}$ is normalized average crack speed. $\Delta l_{bond(BN)}$ is the lattice constant between B-N and B-N bonds. $\Delta l_{bond(CC)}$ is the lattice constant between C-C and C-C bonds. $\Delta l_{bond(BC)}$ is the lattice constant between B-C and B-C bonds. t_1 is the moment when the bond breaks. t_2 is the moment when the bond breaks in the next crack tip path. $V_{bond(BN)}$, $V_{bond(BC)}$ and $V_{bond(CC)}$ are the average crack speed of B-N, B-C and C-C bonds, respectively. $V_{bond(max)}$ is maximum value of crack speed in simulated model.

QUANTIFICATION AND STATISTICAL ANALYSIS

The compute stress/atom command in LAMMPS software is used to calculate the atom stress. To obtain the stress-strain curves during deformation, the atomic stress of individual atoms in the bilayer G/BN mixed heterostructures with CNT was calculated according to the following Equation 31:

$$\sigma_{\varsigma\psi} = \frac{1}{\Omega^{\alpha}}\left(\frac{1}{2}m^{\alpha}v_{\varsigma}^{\alpha}v_{\psi}^{\alpha} + \sum_{\beta = 1,n} r_{\alpha\beta}^{\psi}f_{\alpha\beta}^{\varsigma}\right) \qquad \text{(Equation 31)}$$

Where ς and ψ denote the indices in the Cartesian systems; α and β are the atomic indices; m^{α} and v^{α} denote the mass and velocity of the atom α, respectively; $r_{\alpha\beta}$ is the distance between the atoms α and β; and Ω^{α} is the atomic volume of the atom α. After the stress of each atom is obtained, the average stress of the G/BN mixed heterostructures with CNT is statistics by calculating all the atoms in the system. The failure strain is calculated by multiplying the strain rate of 0.001 ps^{-1} by the time step (ps). Therefore, the stress-strain curve can be drawn by counting the failure strain and the average stress.

The failure stress is considered as the peak of the stress-strain curve. The obtained data are plotted as visualization curves and column charts by Origin software, as shown in the failure stress and strain of Figures 6 and 10 in this paper.

Next, the factor of stress attenuation of failure stress and strain at temperature area per K, including 300–400K, 400–500K, 500–600K, 600–700K and 700–800K, was calculated by the obtained data (failure stress and strain) in Figure 10. For example, the factor of stress attenuation of failure stress in 300-400 K was calculated by using following Equation 32

$$\frac{\sigma_{400K} - \sigma_{300K}}{100} \qquad \text{(Equation 32)}$$

Where σ_{400K} and σ_{300K} are the failure stress at 400 and 300 K, respectively. The unit of 100 is K, which belongs to the range of 300 K-400 K. The factor of stress attenuation of failure strain is also calculated by using following Equation 33

$$\frac{\varepsilon_{400K} - \varepsilon_{300K}}{100} \qquad \text{(Equation 33)}$$

Where ε_{400K} and ε_{300K} are the failure strain at 400 and 300 K, respectively. Similarly, the factor of stress attenuation of failure stress and strain at other temperature area per K are also calculated in this way. Then, the obtained data for the factor of stress attenuation of failure stress and strain at temperature area per K is shown in Figure 11.

The changes of bond length and bond angle is calculated by LAMMPS software. Futhermore, the bond length distributions of LAMMPS simulation system is output and count by bond analysis modifier in Ovito software, the change of the bond angle is count by VMD software. The obtained data ($r_{G\sim bond}$, $r_{BN\sim bond}$, $\Phi_{G\sim angle}$ and $\Phi_{BN\sim angle}$) was conducted based on Equations 19, 20, 21, and 22. Next, the normalized differential value (η) between bond lengths and bond angles related to strain can be calculated by using the Equations 25 and 26.

The obtained normalized differential values (η) between bond length and bond angle of G/BN-CNT heterostructures are plotted as visualization curves in Figure 13.

Validation test

This study and previous studies have analyzed the Young's modulus, failure stress, and failure strain values of single-layer graphene, hBN, and G/BN. These data may be found in Tables S3–S5.[56–59] This is performed to verify the accuracy of the MD models' outcomes. The three mechanical values of single-layer planar G/BN heterostructures demonstrate a significant degree of rationality.

The Young's modulus and failure stress of G/BN in simulated studies have been measured as 821 GPa and 115 GPa, respectively. The simulated results corroborate the findings of Eshkalak et al., who reported Young's modulus and failure stress values of 769 and 127 GPa, respectively, for G/BN heterostructures. In addition, the simulated characteristics of single-layer graphene and hBN show a strong agreement with the previous molecular dynamics discoveries.[56–59]